Numerical and experimental study on silicon microresonators based on phononic crystal slabs with reduced central-hole radii

2013 J. Micromech. Microeng. 23 065030

(http://iopscience.iop.org/0960-1317/23/6/065030)

IOP PUBLISHING JOURNAL OF MICROMECHANICS AND MICROENGINEERING

J. Micromech. Microeng. **23** (2013) 065030 (14pp) doi:10.1088/0960-1317/23/6/065030

Numerical and experimental study on silicon microresonators based on phononic crystal slabs with reduced central-hole radii

Nan Wang[1,2], Fu-Li Hsiao[1,3], J M Tsai[2], Moorthi Palaniapan[1], Dim-Lee Kwong[2] and Chengkuo Lee[1,4]

[1] Department of Electrical and Computer Engineering, National University of Singapore, 4 Engineering Drive 3, Singapore 117576
[2] Institute of Microelectronics, A*STAR (Agency for Science, Technology and Research), 11 Science Park Road, Singapore 117685
[3] Graduate Institute of Photonics, National Changhua University of Education, No. 1, Jin-De Road, Changhua City, 500, Taiwan

E-mail: elelc@nus.edu.sg

Received 7 February 2013, in final form 17 April 2013
Published 16 May 2013
Online at stacks.iop.org/JMM/23/065030

Abstract
In this paper, we report the numerical and experimental study on micromechanical resonators which are made by introducing defects on an otherwise perfect two-dimensional (2D) silicon phononic crystal (PnC) slab. The 2D PnC slab is made by etching a square array of cylindrical air holes in a free-standing silicon plate with a thickness of 10 μm, while the defects are created by reducing the radii of three rows of air holes at the centre of the 2D PnC slab. Three resonators with different values of reduced radii, i.e., 2 μm, 4 μm and 6 μm, are included in this study. The finite-element-modelling method is used to calculate the band structure of the perfect 2D PnC slab and to analyse the different mode shapes of the structure. The design, numerical modelling, fabrication process, as well as characterization results and discussions of the three PnC resonators are also included. Due to its CMOS-compatibility, aluminium nitride is chosen to be the piezoelectric material of the inter-digital transducers, which are used to generate and detect acoustic waves. Testing is done to characterize the resonant frequency (f), quality factor (Q), as well as insertion loss of each of the three microfabricated PnC resonators and the results are discussed by analysing the simulated transmission spectra, the defected band structures, and the steady-state displacement profiles of the structures at their respective resonant frequencies. The experimental results show that the designed PnC resonators with reduced central-hole radii have higher resonant frequency and higher quality factors as compared to their normal Fabry–Perot counterpart, thanks to the higher-frequency modes supported within the cavity and slow sound effect in the lateral direction introduced by the central holes with reduced radii, respectively. As a result, the achieved (f-Q) product can be as high as 2.96×10^{11}, which is among the highest for silicon resonators operating in air.

(Some figures may appear in colour only in the online journal)

[4] Author to whom any correspondence should be addressed.

1. Introduction

During the past two decades, the propagation of acoustic waves in phononic crystals (PnCs) has received a great deal of research attention because of their renewed physical properties and potential applications [1–11]. PnCs are also referred to as phononic band gap (PnBG) materials or acoustic band gap (ABG) materials, whereby a periodic array of scattering inclusions located in a homogeneous background material leads to the formation of PnBG or ABG, prohibiting elastic waves of certain frequencies from travelling in any direction. From the view of the material compositions, PnCs can be classified into three main groups, i.e., solid scattering inclusions in a solid background [5, 10, 12], air scattering inclusions in a solid background [7, 13, 14], and vertical pillars on top of a substrate [15–17]. From the view of the geometry of the structures, three-dimensional (3D) PnC substrate [4], 2D PnC slabs [5, 7, 18] and one-dimensional (1D) PnC strips [19–21] have also been reported, of which the 2D PnC slab is gaining more and more research interest because of the better capability to trap the elastic energy within the structure provided by the 2D nature of the PnC slabs. Various configurations of PnC slabs, such as air holes drilled on a 2D silicon membrane [7], cylindrical rods deposited on the top of the membrane [12], cylindrical rods inserted into the air holes [5, 22], as well as inverse acoustic band gap (IABG) structure [23], have been reported by various research groups. When various types of defects are introduced to an otherwise perfect PnC structure, devices of different functionalities like resonators and waveguides have been reported as well [24–34]. For example, a line defect can also be introduced along the direction of wave propagation to form a waveguide [26], a cavity-mode resonator can be formed by adding a line defect perpendicular to the direction of wave propagation in the form of a Fabry–Perot structure [34], and Bloch-mode resonators which are formed by adding an extra row of air holes [33] or introducing alternate defects [31, 32] to the Fabry–Perot resonant structure are also proposed to solve the trade-off [35] between quality factor and motional impedance. Such trade-off is typically reported in capacitive-based [36–41] and piezoelectric-based [42–44] devices.

From the aspect of the dispersion properties, PnBG is the frequency range which no elastic vibrating modes can be supported within. Analogically to the well-known photonic crystals (PhCs) [45, 46] which are formed by a periodic dielectric in electromagnetic medium, PnCs are inhomogeneous materials with periodic variations in the acoustic medium. In PhC, researchers have already demonstrated that the scattering loss in Fabry-Perot micro/nano cavity structure [47, 48] is high due to the abrupt terminations of the two edges of the Fabry–Perot resonant cavity, which subsequently renders a lower quality factor (Q) achieved as the Q is inversely related to the amount of energy loss. To overcome this problem, Lalanne *et al* proposed that the resonant cavity should be created by modifying portions of the lattice structure, instead of completely removing the scattering inclusions [49]. This is because the wave penetrates some distance into the edge of the cavity instead of being reflected exactly at the edge. It is crucial that the supported mode does not abruptly terminate at the cavity boundary but penetrates and exponentially decays outside the cavity, as abrupt termination would lead to a significant amount of scattering loss [49]. By analogy, if the air holes in the PnC are partially modified instead of being completely removed, the scattering loss can also be reduced and Q can be enhanced.

In this paper, we report numerically and experimentally the micromechanical resonators formed by reducing the radii of three rows of air holes at the centre of the 2D silicon PnC slab of square lattice with a thickness of 10 μm. This design approach of reducing the central-hole radii is adopted in order to reduce the scattering loss and enhance Q. Three resonators with different values of reduced radii, including 2 μm, 4 μm and 6 μm, are investigated in this study. A Fabry–Perot PnC resonator which was reported previously [34] with three rows of air holes completely removed from the centre of the 2D silicon PnC slab is also included in this paper for reference. Prior to the resonator design, several silicon/air square lattice PnCs with different parameters are analysed by finite-element-modelling (FEM) and their performances are optimized between the width of the band gap and the challenge to the microfabrication capability. The detailed fabrication process is discussed and the microfabricated resonators with high-Q resonant peaks in the hundred MHz range are characterized in terms of the resonant frequency (f), quality factor (Q), as well as insertion loss (IL). The experimental results are discussed by using different FEM approaches to analyse the transmission spectra, the defected band structures, and the steady-state displacement profiles of the structures at their respective resonant frequencies.

2. Modelling and design

In the phononic structure, a phononic band gap can be formed when scattering inclusions arranged periodically in a homogeneous host material cause waves in certain frequencies to be completely reflected by the structure. When defects are introduced to the otherwise perfect PnC structure by making the radii of the central rows of inclusions different from the inclusions of the surrounding PnC structure, a resonant peak can then appear within the stop band to form a PnC resonator.

2.1. PnC band gap optimization

The band structure of the perfect 2D PnC slab is analysed by FEM using the eigenfrequency solver in the ‘piezo solid’ model of COMSOL Multiphysics software. The main principle governing the FEM of the band structure is derived from first-principles physics, i.e., the combination of Newton’s Second Law of motion and a constitutive relation. The detailed equations which govern the calculation of the band structure are reported in our previous work [33] and the FEM approach is similar to the modelling approach described in [33] and [34], which starts with the construction of a unit cell of the 2 D PnC slab as depicted in figure 1(a). In the subdomain settings of the COMSOL FEM, parameters which describe the material properties, such as elasticity matrix, coupling

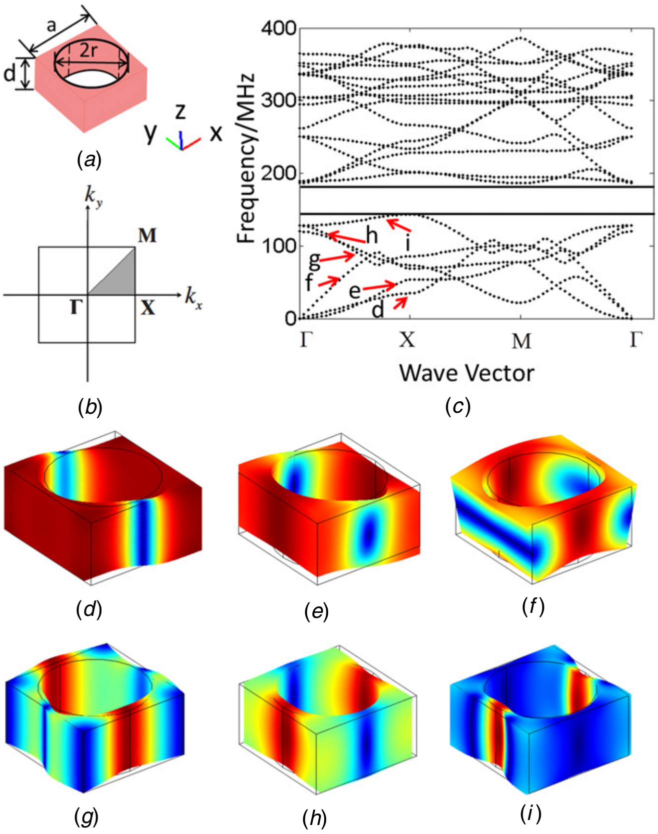

Figure 1. (*a*) Schematic drawing of the unit cell of the structure for band gap calculation. (*b*) Schematic drawing of the first Brillouin zone. Shaded area indicates the irreducible part of the first Brillouin zone. (*c*) The band structure of the phononic crystal structure with $d = 10\ \mu$m, $r = 8\ \mu$m and $a = 18\ \mu$m, which gives $r/a = 0.45$ and $d/a = 0.55$. (*d*)–(*h*) Mode shapes of the first six modes as labelled in (*c*).

matrix, relative permittivity and material density are entered to define the structure of air holes in the Si background. Zero charge/symmetry is applied for the electric boundary condition on all the exterior boundaries and point-to-point periodic boundary conditions are applied along x and y directions. As a PnC slab is formed by a periodic array of scattering inclusions located in a homogeneous background, it can also be considered as a periodic repetition of the unit cell shown in figure 1(*a*). Therefore, periodic boundary conditions can be applied along the x direction (on the two faces which are parallel to the y-z plane) and the y direction (on the two faces which are parallel to the x-z plane) of the unit cell (figure 1(*a*)) to simulate an infinite repetition of the unit cell along the x and y directions, according to the Bloch-Floquet theorem:

$$u_i(x + a, y + a) = u_i(x, y) \exp[-j(k_x a + k_y a)]$$

where u is the displacement vector, $i = x, y, z$, whereas k_x and k_y are the Bloch wave vectors in the x and y directions, respectively, and a is the lattice constant along the x and y directions which are the same, as the structure is of square lattice. In this case, since the structure to be simulated is formed by the infinite repetition of the unit cell along the x and y directions but no repetition along the z direction, it has finite thickness in the z direction but infinite length along the x and y directions. Therefore, we are effectively simulating a 2D structure using a 3D unit cell. Lastly we sweep the wave vector along the irreducible part of the first Brillouin zone (grey area of figure 1(*b*)) and combine all the eigenfrequencies computed by the eigenfrequency solver to generate the band structure. Figure 1(*c*) shows the band structure of a square-lattice perfect PnC after the optimization of various parameters and the detailed optimization process will be discussed later in this section. The mode shapes of the first six modes in the band structure as labelled from d to i in figure 1(*c*) are shown from figures 1(*d*)–(*i*), respectively. From the calculated mode shapes, it can be clearly seen that figure 1(*d*) shows the in-plane transverse mode, figures 1(*e*) and (*f*) show the out-of-plane transverse mode, figure 1(*g*) shows a combination of longitudinal mode and in-plane transverse mode, and figures 1(*h*) and (*i*) show the longitudinal mode.

From the schematic drawing of the unit cell depicted in figure 1(*a*), a is the lattice constant (pitch) which means the distance between the centres of two adjacent holes in the square lattice, d is the thickness of the PnC slab and r is the radius of the air holes. In the FEM process to calculate the band structure, only one unit cell is needed as point-to-point periodic boundary conditions are applied along the x and y directions to simulate the repetition of the unit cell infinitely along the x and y directions. For our band gap optimization process, we explored the effect of r/a ratio and d/a ratio on the band structure by fixing d at 10 μm and varying r and a. From the derived results shown in figure 2, first of all, the width of the band gap gradually increases with r/a while keeping d/a constant (figure 2(*a*)). Secondly, as shown in figure 2(*b*), when keeping r/a as a constant of 0.475, the width of the band gap reaches its maximum value at around $d/a = 0.57$. Then the width of the band gap decreases with increased d/a when d/a is greater than 0.57. Hence, given the fixed thickness of $d = 10\ \mu$m, the maximum band gap can be achieved when $a = 17.54\ \mu$m, which means $d/a = 0.57$ (according to the results shown in figure 2(*b*)). By the simulation results in figure 2(*a*), maximum band gap can be achieved when $r/a = 0.47$. However, this will render the diameter of air holes to be 16.49 μm, if a is chosen to be 17.54 μm. As a result, the minimum feature size or the critical dimension (CD), which is the minimum width of silicon between two adjacent air holes in this case, is 1.05 μm. Considering the drift and the side wall profile of the deep reactive ion etching (DRIE) process, such a small feature size is difficult to be fabricated and the CD control is also very difficult. Therefore, we set $r = 8\ \mu$m and $a = 18\ \mu$m as our target values in the actual microfabrication. This gives us $r/a = 0.45$, which still yields a reasonably wide band gap while keeping the microfabrication process less challenging and the CD control easier to achieve. The calculated band structure after optimization shown in figure 1(*c*) has a stopband extending from 143.3 MHz to 186.3 MHz, rendering the width of the band gap to be 43 MHz and the gap-to-midgap frequency ratio to be 26.1%.

2.2. PnC resonator structure design

After optimizing the band structure, the optimized parameters, i.e., $r = 8\ \mu$m and $a = 18\ \mu$m, are used as the basis for the

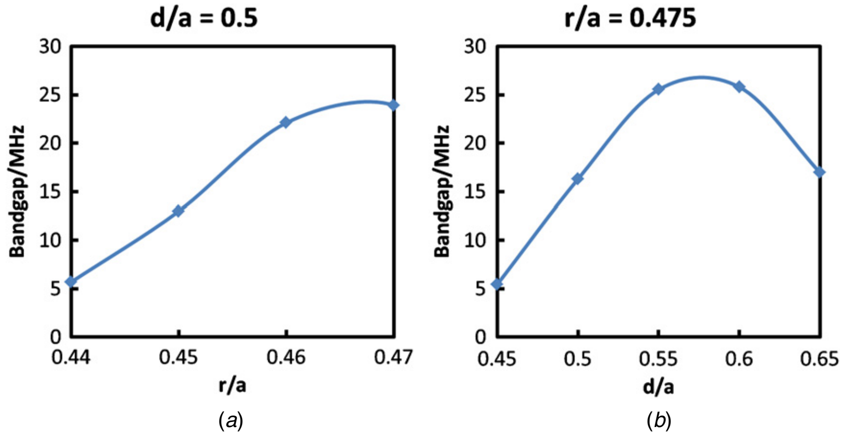

Figure 2. Band gap optimization by (*a*) keeping $d/a = 0.5$ and varying r/a (*b*) keeping $r/a = 0.475$ and varying d/a. d is fixed at 10 μm for both cases.

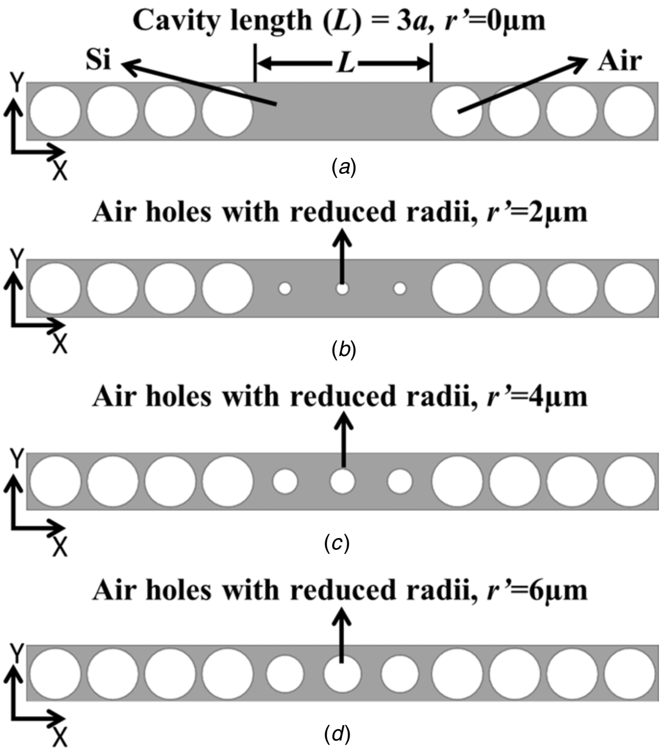

Figure 3. Schematic drawings of the supercell of the (*a*) the Fabry–Perot PnC resonator with three rows of air holes completely removed at the centre of the PnC region (*b*) the PnC resonator with reduced radii of $r' = 2$ μm for the central three rows of air holes (*c*) the PnC resonator with reduced radii of $r' = 4$ μm for the central three rows of air holes (*d*) the PnC resonator with reduced radii of $r' = 6$ μm for the central three rows of air holes. The supercells repeat themselves in the *y* direction in the microfabricated devices and the acoustic waves travel along the *x* direction.

design of the PnC resonators. Our design approach here is to modify portions of the perfect PnC structure, instead of completely removing some of the air holes, in order to reduce the scattering loss which is a major source for energy loss. As a result, the Q can be enhanced as Q is inversely related to the amount of energy loss. Figures 3(*b*)–(*d*) show the schematic supercells of the designed resonators with reduced radii of $r' = 2$ μm, $r' = 4$ μm and $r' = 6$ μm, respectively, for the three rows of air holes at the centre of the PnC. For the purpose of easy comparison between the Fabry-Perot resonators and the designed resonators with reduced central-hole radii, we also include the supercell for the case of $r' = 0$ μm (figure 3(*a*)) which is essentially the Fabry-Perot PnC resonator reported in our previous work [34]. The grey region represents the silicon background and the white circles represent air holes. The supercells repeat themselves in the *y* direction in the microfabricated devices and the acoustic waves travel along the *x* direction. For all the four cases, since the number of rows of air holes being removed or modified is three, the cavity length (L) is $3a$, which means three times the lattice constant. As all the resonators have the same basic parameters ($r = 8$ μm, $a = 18$ μm, and $d = 10$ μm) and the same cavity length of $3a$, the differences in their performance will be solely caused by the configurations of the central defected region.

3. Microfabrication

The top-down CMOS-compatible microfabrication process which requires four photolithography masks (figure 4(*a*)) follows partially from our previous work [33], but improvements and modifications in the detailed fabrication steps were made to further optimize the CD control and other fabrication qualities for the new batch of fabricated devices.

The process starts with silicon-on-insulator (SOI) wafers with a device layer thickness of 10 μm, the buried oxide (BOX) layer thickness of 1 μm and silicon handle layer thickness of 750 μm. First, AlN of 1 μm thickness is deposited using radio frequency (RF) sputtering. Next, a layer of SiO_2 with 1 μm thickness is deposited using plasma enhanced chemical vapour deposition (PECVD) and dry etched to serve as a hard mask to define the subsequent etching of AlN. After the PR is stripped, the deposited AlN layer is then patterned subsequently with a SiO_2 hard mask, using dry etch with a combination gas of $Cl_2/BCl_3/Ar$ (the ratio of the gas flow is 100:55:15) in an AMAT Centura ECR (Electro Cyclotron Resonance) etcher (model: 5200, chamber pressure: 11mT, bias voltage: −1000 V, RF power: 1300 W), using an endpoint based recipe to detect etch completion with an endpoint detection mechanism, so that over etching of silicon device

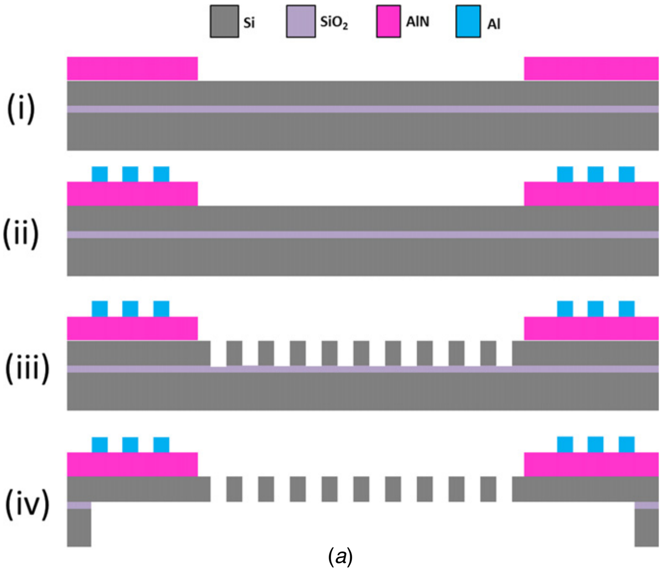

(*a*)

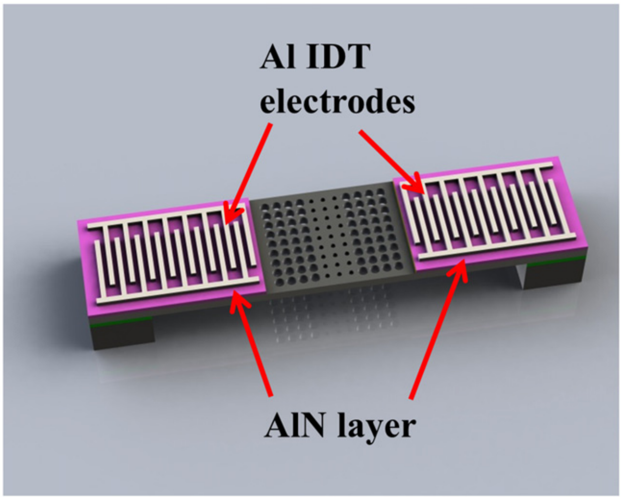

(*b*)

Figure 4. (*a*) CMOS-compatible microfabrication process starting from the SOI wafer: (i) AlN deposition and patterning, (ii) top Al electrode deposition and patterning, (iii) phononic crystal formation by DRIE through the device layer, (iv) backside release by DRIE of substrate and RIE of BOX layer. (*b*) The schematic drawing of a typical PnC resonator structure with reduced central-hole radii after all the fabrication process.

layer is minimized. The etched AlN layer is to serve as the piezoelectric layer for the Inter-Digital Transducer (IDT) (figure 4(*a*)(*i*)). Instead if using PR, the extra layer of SiO_2 is used as a hard mask to etch AlN in order to supress the polymer formation on the sidewall of the AlN which occurs when PR is used to etch AlN with the aforementioned recipe. The process continues by the deposition of the Al layer of 0.5 μm thickness and patterning using a similar etching process as in etching AlN (in AMAT Centura ECR with Cl_2:110sccm, Ar: 15 sccm, RF power: 150 W, chamber pressure: 10 mT, bias voltage: -1250 V, endpoint based recipe) to form IDT which acts as the input and output of the phononic structure to launch and detect acoustic waves along the x direction (figure 4(*a*)(*ii*)). The etching of Al does not need a SiO_2 hard mask as the etching of Al using PR does not form polymer on the sidewall. Then, cylindrical air holes in a square lattice are patterned to form the phononic structure by Deep Reactive Ion Etching (DRIE) through the silicon device layer (figure 4(*a*)(*iii*)). The etching is done in an STS Inductively Coupled Plasma (ICP) etcher with an 11 s etching cycle (etch gas: SF_6, flow rate: 110 sccm, RF power: 15 W, chamber pressure: 10 mT, helium cooled chuck) and a 5 s passivation cycle (passivation gas: C_4F_8, flow rate: 80 sccm, RF power: 600 W, chamber pressure: 10 mT, helium cooled chuck). As the radius of the central holes for some PnC resonator (r') is much smaller than the radius of the PnC structure (r), e.g. the case of $r' = 2$ μm, 120% over-etching using reduced RF power (RF etching power: 2W, RF passivation power: 400 W) is done to minimize the micro-loading effect. We also use a slower recipe for silicon etching by reducing the RF power to ensure a straight sidewall profile. Lastly, the wafer is flipped and the whole structure becomes a free-standing 2D phononic slab by DRIE on the backside (figure 4(*a*)(*iv*)) after grinding the wafer from backside to reduce the thickness of the wafer to 500 μm. At this step, it is better not to grind the wafer too thin for easy handling purposes. The releasing process involves two steps: DRIE of grinded silicon substrate and Reactive Ion Etching (RIE) of the BOX layer, both from the backside. The RIE of the BOX layer is done in a Plasma-Therm RIE etching chamber (etching gas: CF_4/O_2, flow rate: 15 sccm/3 sccm, RF power: 200 W, chamber pressure: 15 mT, helium cooled chuck). The schematic drawing of a typical PnC resonator structure with reduced central-hole radii after all the fabrication process is shown in figure 4(*b*), with IDT formed by piezoelectric AlN layer and an Al electrode on the two sides of the air/silicon phononic structure.

Figure 5(*a*) shows the SEM image of the Fabry–Perot PnC resonator from our previous work [34] which is formed by completely removing three rows of air holes at the centre of the PnC region. We include it here to serve as a reference for the comparison between the performance of the Fabry–Perot PnC resonator and the PnC resonators with reduced central-hole radii. Figures 5(*b*)–(*d*) show the SEM images of the designed PnC resonators with reduced central-hole radii of $r' = 2$ μm, $r' = 4$ μm and $r' = 6$ μm, respectively. Four periods (rows) of air holes are patterned on each side of the defect region for all the PnC resonators, and IDT are formed by a piezoelectric AlN layer and an Al electrode on the two sides of the air/silicon phononic structure. The IDT employed for this study has a periodicity of 15 μm and a finger width of 7.5 μm, rendering the metallization ratio of the transducer to be 50%. The length of the IDT is 150 μm. The PnC region inside the solid red square in figure 5(*b*) is the typical supercell structure shown in figure 3(*b*) and the supercell is also used for the FEM simulation which will be discussed later in this manuscript. From the SEM images, it can be shown that the actual microfabricated PnC structures are a repetition of various supercells along the y direction and acoustic waves travel along the x direction. Due to the piezoelectric properties of the AlN film, acoustic waves are launched toward the PnC structure along the x direction when an AC signal is applied on the IDT of the input port. As the piezoelectric AlN film can convert the displacements caused by transmitted acoustic

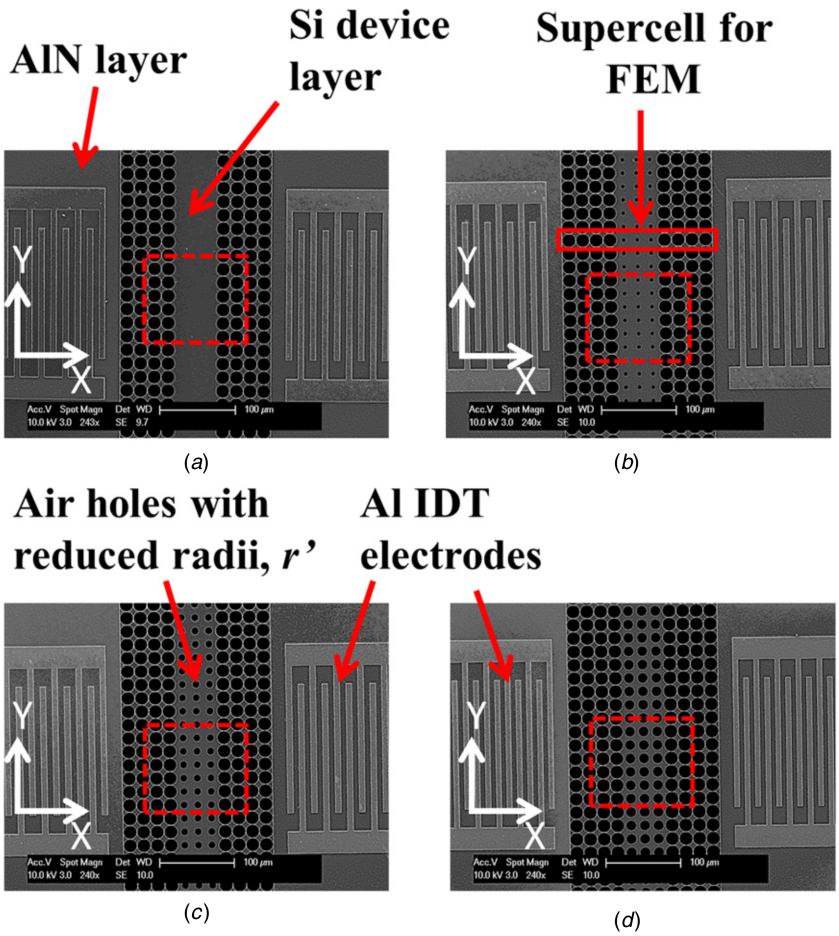

Figure 5. SEM images of (*a*) the Fabry-Perot PnC resonator (*b*) the PnC resonator with reduced central-hole radii of $r' = 2\ \mu$m (c) the PnC resonator with reduced central-hole radii of $r' = 4\ \mu$m (*d*) the PnC resonator with reduced central-hole radii of $r' = 6\ \mu$m. Elastic waves travel along the *x* direction in all microfabricated devices. The scale bar in each of the SEM image represents 100 μm. Areas in dashed squares are the region to be zoomed in and the close-up views are shown in figure 6.

waves into electrical signals, the transmitted acoustic waves through the PnC structure could be picked up by the IDT of the output port on the other side of the phononic structure, after their interaction with the PnC structure. Figure 6 shows the close-up views of the defected regions at the centre of the PnC, which are the areas enclosed by the dashed squares in all sub-figures in figure 5.

Figure 7 shows an even closer look at the air holes after the silicon device layer DRIE process, in order to examine the effects of over etching and micro loading. For over etching, we reduced the RF etching power to 2 W and the RF passivation power to 400 W, in order to minimize the micro-loading effect and the unintended etching to the underlying SiO_2 layer. As the RF etching power is reduced very significantly while the passivation power is reduced only slightly, the passivation cycle during the over-etching process offers excellent protection of the side wall against etching during the etching cycle. Furthermore, our silicon DRIE recipe has a selectivity of 330:1 over the BOX layer underneath the silicon device layer. Therefore, the effect of over etching on the diameter of various holes is negligible. Also, the unintended etching to the underlying SiO_2 layer is also minimized. From the SEM image shown in figure 7, the side wall profile is very straight, showing excellent protection of the side wall against over etching. Nevertheless, the scallop pattern in the sidewall during the DRIE process can still be observed and it causes the drift in CD control, which will lead to the drift in the performance of the resonators from the desired value. In addition, as the releasing DRIE process is done on the backside of the wafer, we deposited a layer of SiO_2 on the front side of the wafer to protect the silicon device layer with PnC structures on it from breaking during the releasing DRIE process. After the DRIE process, the layer of protecting SiO_2 is then etched away by vapour hydrofluoric acid (VHF) to expose the underneath silicon device layer. This additionally deposited SiO_2 layer serves as a protection layer which not only protects the underneath silicon device layer from breaking after the structure was released, it also protects the front side of the silicon device layer from scratching and damaging by the machine during the DRIE process on the back side.

Another common concern for the fabrication of the 2D suspended membrane structure is the curvature of the membrane after releasing. To access the curvature of our PnC resonators, we also measured the surface profiles of the PnC structure and the free-standing silicon slab without any PnC structure using Veeco Wyko Non-contact Profilometer and the measured profiles are shown in the figure 8, with the

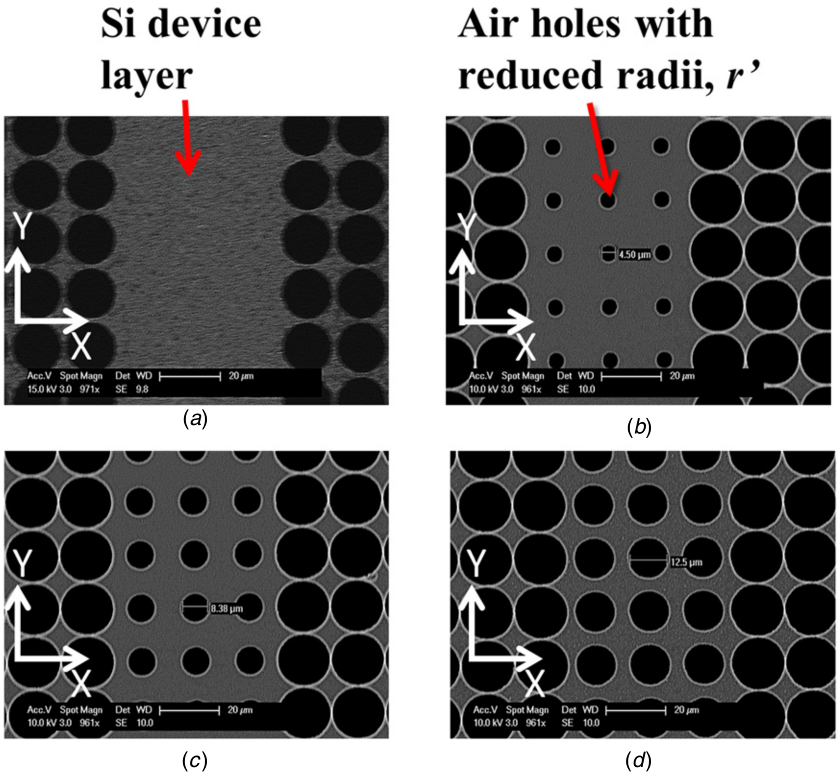

Figure 6. Close-up views of the central defected regions of (*a*) the Fabry–Perot PnC resonator, (*b*) the PnC resonator with reduced central-hole radii of $r' = 2\ \mu$m, (*c*) the PnC resonator with reduced central-hole radii of $r' = 4\ \mu$m, (*d*) the PnC resonator with reduced central-hole radii of $r' = 6\ \mu$m. The scale bar in each of the SEM image represents 20 μm.

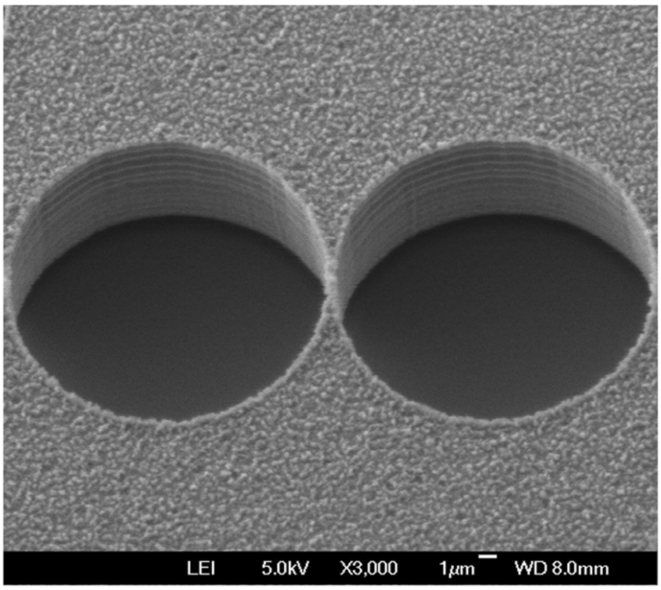

Figure 7. More zoomed-in view of the air holes after the silicon device layer DRIE process, in order to examine the effects of over etching and micro loading.

surface profile of the free-standing silicon slab without any PnC structure shown in figure 8(*a*) and the surface profile of the PnC structure shown in figure 8(*b*). From the two figures, we can see that the height differences for both the free-standing PnC membrane and the silicon slab without any PnC structure are around 100 nm. Given that the thickness of the Si device layer is 10 μm, the height difference is only 1% of the device layer thickness, which can be safely neglected. Therefore, the curvature of the free-standing slab after releasing is also negligible, which also indicates that the stress level of the released membrane film is very low. Due to the low stress level, the DRIE released membrane is not easily broken.

Therefore, for our fabricated resonator structures, the curvature for the free-standing slab after releasing is negligible because the area of the silicon handle layer which is exposed for etching during the releasing process is only the area directly under the phononic structure. At the chip level or the wafer level, the area exposed for releasing, which is actually the area of free-standing slab, only occupies less than 10% of the total wafer or chip area. In other words, the free-standing slab is actually a small area of silicon membrane which is bounded by a large area of surrounding unreleased silicon. Moreover, our Si DRIE process requires that the total area exposed for Si etching should be less than 15% of the total wafer area, in order to achieve a straight side wall profile and good etching uniformity across the wafer. Also, if the area exposed for Si etching is too large, the whole wafer becomes fragile after releasing as the device layer is only 10 μm. Therefore, the free-standing silicon slab is fixed by the surrounding unreleased silicon to prevent any curvature or breakage.

4. Device characterization and discussions

To experimentally characterize the microfabricated PnC devices, a network analyser (Model: Agilent E8364B) is

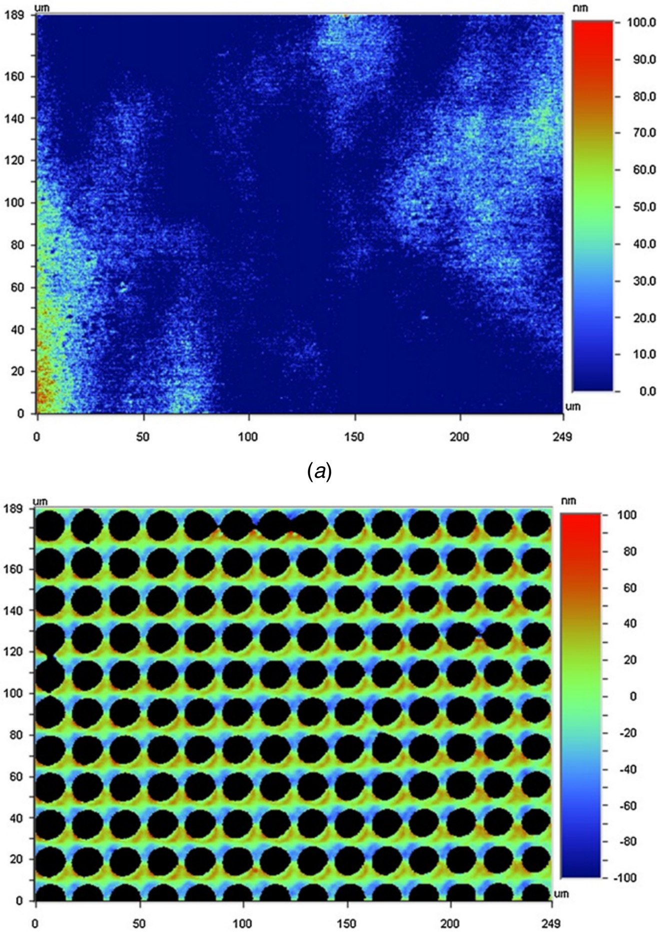

(*b*)

Figure 8. Surface profiles measured by Veeco Wyko Non-contact Profilometer for (*a*) the free-standing silicon slab without any PnC structure, (*b*) the optimized PnC structure.

used after performing a standard Short-Open-Load-Through calibration. The testing setups and testing procedures are the same as those reported in our previous work [33, 34], so they will not be repeated for simplicity. We also include a free-standing silicon slab without any PnC structure and with the same length of wave propagation and in the same frequency range for normalization purposes. Therefore, when the frequency-response transmission spectra of various PnC resonators are normalized with respect to the pure silicon slab (the normalization structure), the influences of the air surrounding the structure, together with other parasitic effects caused by the IDTs, are eliminated. In this case, the resultant transmission spectra of various designed resonators after normalization are solely due to the effects of the PnC structure with air holes in a homogeneous silicon background, which have been considered during the FEM as it sets the air holes in silicon background in the simulation settings.

Figure 9(*a*) shows the measured transmission spectrum of the free-standing silicon slab without any PnC structure and figure 9(*b*) shows the transmission spectrum of the perfect PnC structure after the optimization of the lattice parameters. We observed that the measured stopband of 140 MHz $< f < 195$ MHz agreed quite well with the frequency range of the band gap in the calculated band structure shown in figure 1(*c*). We believe the discrepancies are due to the drift of CD control in microfabrication process, in which the radii of the air holes in microfabricated devices are larger than designed. The measured stopband leads to the centre frequency of 167.5 MHz and gap-to-midgap frequency ratio of 32.8%. Figure 9(*b*) also shows a maximum attenuation of 30 dB within the stopband.

Figure 10(*a*) reproduces the measured transmission spectrum of the PnC Fabry–Perot resonator (figure 5(*a*)) from our previous work [34], with three rows of air holes completely removed ($L = 3a$) at the centre of the PnC region. Figures 10(*b*)–(*d*) show the measured transmission spectra of the PnC resonator with a reduced radii (r') of the central three rows of air holes ($L = 3a$) of (b) $r' = 2$ μm (figures 5(*b*)) and (*c*) $r' = 4$ μm (figures 5(*c*)), and (*d*) $r' = 6$ μm (figure 5(*d*)), respectively. From the measured transmission spectra shown in figure 10, it can be shown that for the same cavity length, all the PnC resonators with reduced central-hole radii have higher f and higher Q as compared to their Fabry–Perot counterpart. The Fabry-Perot PnC resonator shown in figure 5(*a*) can also be considered as the PnC resonator with a reduced central-hole radii of $r' = 0$ μm. When the central-hole radius increases from 0 μm to 2 μm, the resonant frequency increases sharply from 152.46 MHz to 182.1 MHz, the quality factor also jumps from 1016 to 1624, and the insertion loss decreases from 13 dB to 11 dB. This indicates that the pure Fabry–Perot resonator changed to a completely different mode of operation when additional air holes are introduced in the central cavity region. When r' is further increased to 4 μm, both the resonant frequency and the quality factor drop, to a value of 179.9 MHz and 1086, respectively, while the insertion loss increases to 13.1 dB. This means the optimized condition for the performance parameters as achieved in the case of $r' = 2$ μm is destroyed. When r' is further increased to 6 μm, the resonant frequency drops further to 176.22 MHz but the quality factor increases to 1311, while the insertion loss remains almost unchanged at 13.2 dB.

From the measured transmission spectra, we can calculate the f-Q product, a common figure-of-merit for micromechanical resonators, for the three PnC resonators with a reduced central-hole radii to be 2.96×10^{11}, 1.95×10^{11} and 2.31×10^{11}, for the case of $r' = 2$ μm, $r' = 4$ μm, and $r' = 6$ μm, respectively. These values are among the highest f-Q products for silicon microresonators operating in air. It can also be noticed that the f-Q product of the three PnC resonators with reduced central-hole radii are all larger than the case of the pure Fabry-Perot resonator with the same cavity length ($L = 3a$), which is 1.5×10^{11}. Since all the PnC resonators reported here have the same basic parameters ($r = 8$ μm, $a = 18$ μm, and $d = 10$ μm) and the same cavity length, i.e., $L = 3a$, it can be concluded that the differences in their performance will be solely caused by the configurations of the central defected region. Table 1 below summarizes the performance parameters of all the resonators reported in this manuscript.

The transmission spectra of the designed PnC resonator structure is also analysed by FEM, with a supercell (figure 3) constructed first. Subdomain settings are applied to simulate

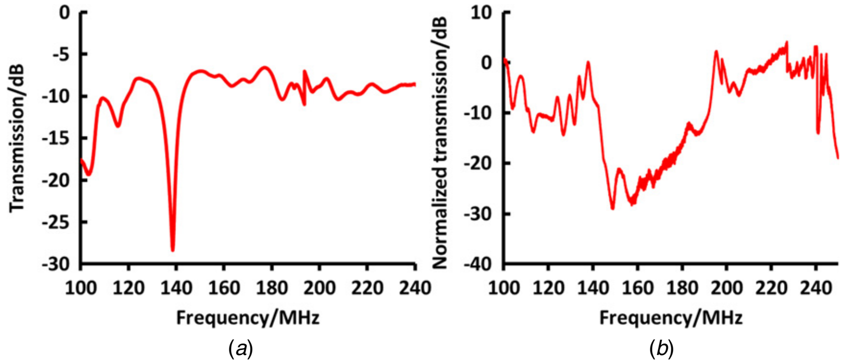

Figure 9. Measured transmission spectra of (*a*) the free-standing silicon slab without any PnC structure, (*b*) the optimized PnC structure.

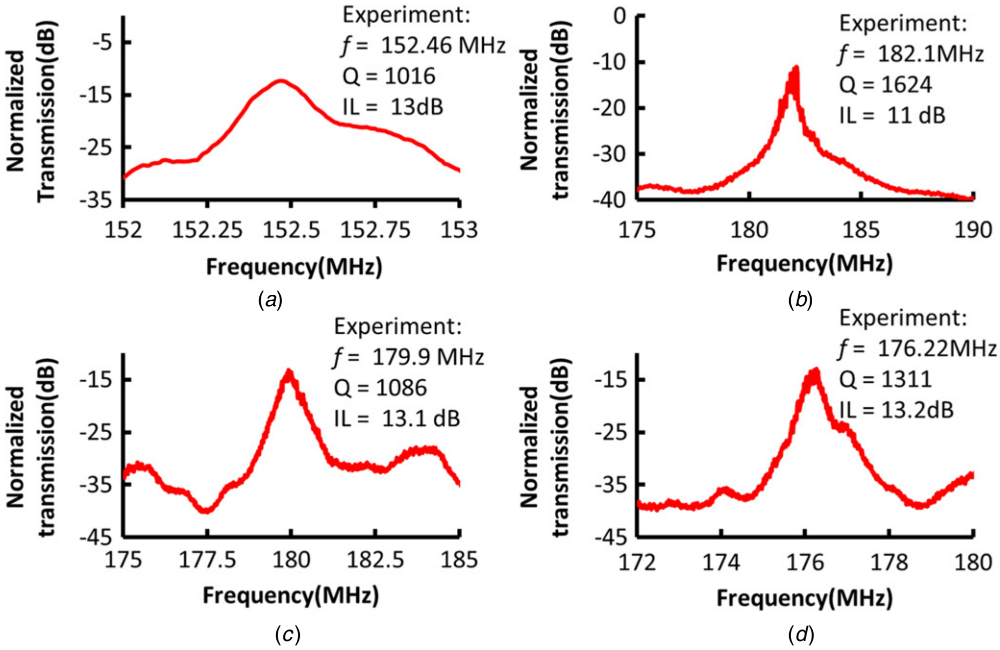

Figure 10. Measured transmission spectra of (*a*) the Fabry–Perot PnC resonator, (*b*) the PnC resonator with reduced central-hole radii of $r' = 2\ \mu$m, (*c*) the PnC resonator with reduced central-hole radii of $r' = 4\ \mu$m, (*d*) the PnC resonator with reduced central-hole radii of $r' = 6\ \mu$m. All the PnC resonators with reduced central-hole radii have a higher f and a higher Q as compared to their Fabry–Perot counterpart.

Table 1. Performance parameters of various resonators.

	r'(μm)			
Performance parameters	0	2	4	6
f (MHz)	152.46	182.1	179.9	176.22
Q	1016	1624	1086	1311
IL (dB)	13	11	13.1	13.2
f-Q product (Hz)	1.5×10^{11}	2.96×10^{11}	1.95×10^{11}	2.31×10^{11}

air holes in the silicon background matrix. For boundary settings, zero charge/symmetry is chosen and force is applied from the left edge of the structure to simulate the acoustic waves generated. Periodic boundary conditions are then applied along the y direction. A frequency response solver is selected as the solving mechanism and the frequency of the input acoustic waves is swept from the lower edge to the upper edge of the band gap of the pure PnC structure (figure 1(*c*)). The acoustic waves after interaction with the phononic structure is collected by a probing tool at the right edge of the structure to calculate the total displacement of the right edge. A flat silicon plate without any PnC structure and with the same length of wave propagation is also constructed for the purpose of normalization. The simulated transmission spectra for the case of the Fabry-Perot resonator is shown in figure 11(*a*), while figures 11(*b*)–(*d*) show the simulated transmission spectra for the PnC resonators with reduced central-hole radii of $r' = 2\ \mu$m, $r' = 4\ \mu$m, and $r' = 6\ \mu$m, respectively. For all four cases, the resonant frequencies in the simulated transmission spectra agree quite well with the experimental results, expect

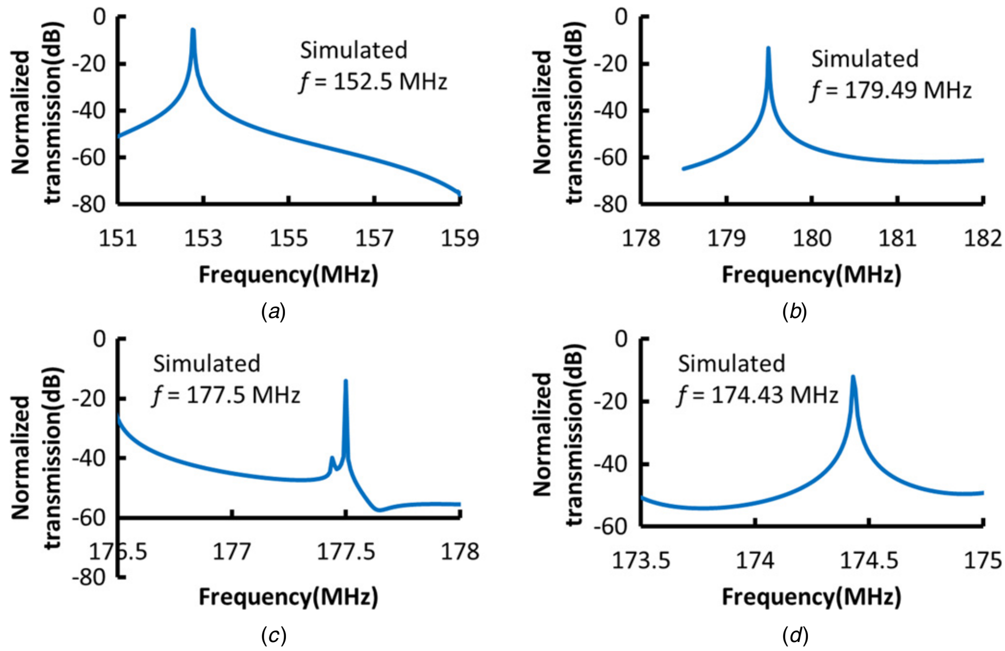

Figure 11. Simulated transmission spectra of (*a*) the Fabry–Perot PnC resonator, (*b*) the PnC resonator with reduced central-hole radii of $r' = 2$ μm, (*c*) the PnC resonator with reduced central-hole radii of $r' = 4$ μm, (*d*) the PnC resonator with reduced central-hole radii of $r' = 6$ μm. The resonant frequencies in the simulated transmission spectra are in very good agreement with the measured data.

for small deviations which are caused by the fabrication error. However, from our previous experience, the simulated transmission spectra are a good estimation of the resonant frequencies but not a good estimation of the quality factors due to the following two reasons. First, the scattering loss, which is a major source of energy loss, is not considered when periodic boundary conditions were applied in the simulation and we assumed the whole resonator is formed by the duplication of the repeating unit in the *y* direction. Second, the loss due to electro-acoustic coupling is not considered when loads are directly applied to the structure in our simulation. However, acoustic waves are launched towards the phononic structure through the piezoelectric effect of IDT in the actual experiment. Therefore, the simulated transmission spectra are good indicators of only the resonant frequencies of various PnC resonators.

In order to analyse the reasons for the different quality factors obtained from different resonators by accounting the scattering loss, the band structures of various PnC resonators are also calculated using similar approach as described in section 2.2. Again, supercells shown in figure 3 are constructed first and periodic boundary conditions are applied along the *y* direction only instead of both the *x* and *y* directions for the case of the perfect PnC structure. The calculated eigenfrequencies are combined to generate the defected band structures for various PnC resonators. In the band structure calculated for the PnC structure, the first order derivative of frequency against wave vector represents the group velocity of the guided mode of the acoustic waves along the waveguide in the lateral direction, which is the *y* direction in our case. Therefore, flatter bands leads to slower group velocities and steeper bands lead to higher group velocities, since the first order derivative of frequency against wave vector is reflected as the slope of that particular band in the band structure diagram. As a result, the group velocity for a completely flat band is equal or close to zero and the modes associated with the flat band have a strong spatial localization [50]. Elastic waves with a small group velocity are called slow sound. Therefore, the phenomenon of the strong spatial localization of elastic waves due to a small group velocity is also called the 'slow sound effect'. On the other hand, a steep band means that the group velocity in the *y* direction is high. From the SEM images shown in figure 5, we can see that for the PnC resonators, the resonant cavity in the *x* direction is essentially a waveguide in the *y* direction with the two ends at the top and the bottom of the resonant cavity being open. In this case, when elastic waves enter the resonant cavity, its associated elastic energy can leak through the open ends at the top and the bottom of the resonant cavity. Therefore, the rate of energy leakage is high when the band is steeper as the group velocity of elastic waves along the *y* direction is high, leading to higher energy loss. On the other hand, when the band is flatter as the group velocity of elastic waves along the *y* direction is low or even zero, elastic waves hardly travel along the *y* direction and stay inside the resonant cavity to be reflected back and forth for a longer period of time, resulting in lower energy loss. Conceptually, the quality factor of a resonator is a direct indicator of the energy loss and is defined as

$$Q = \frac{2\pi \times \text{Energy Stored}}{\text{Energy Disipated}}$$

Therefore, the resonator with a flatter band (lower group velocity of elastic waves along the *y* direction) should have a higher quality factor, due to lower energy loss.

The calculated band structure for the case of the Fabry–Perot resonator is shown in figure 12(*a*), while figures 12(*b*)–(*d*) show the calculated band structures for the PnC resonators with a reduced central-hole radii of $r' = 2$ μm, $r' = 4$ μm,

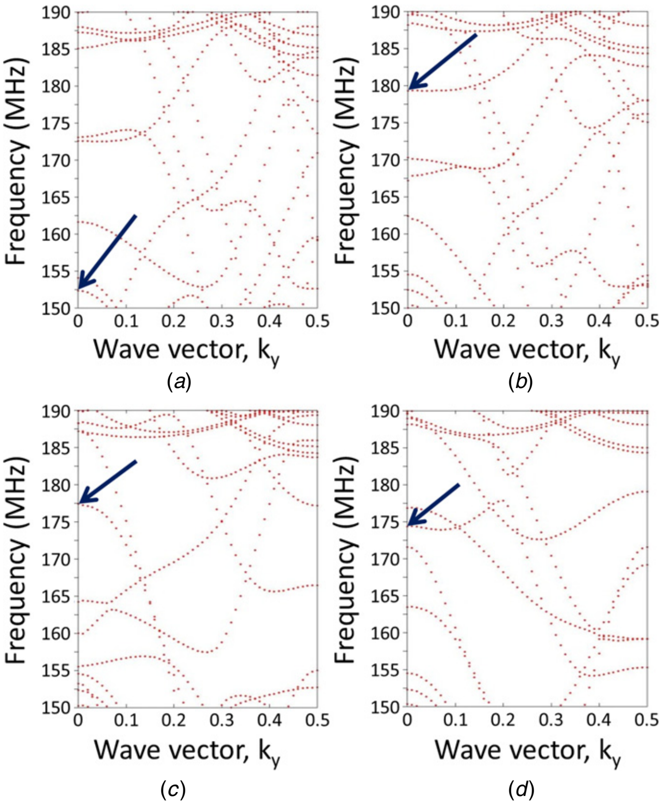

Figure 12. Calculated band structures of (*a*) the Fabry–Perot PnC resonator, (*b*) the PnC resonator with reduced central-hole radii of $r' = 2\ \mu$m, (*c*) the PnC resonator with reduced central-hole radii of $r' = 4\ \mu$m, (*d*) the PnC resonator with reduced central-hole radii of $r' = 6\ \mu$m. The selected bands of interest which correspond to the resonant peaks shown in figure 11 are labelled using blue arrows.

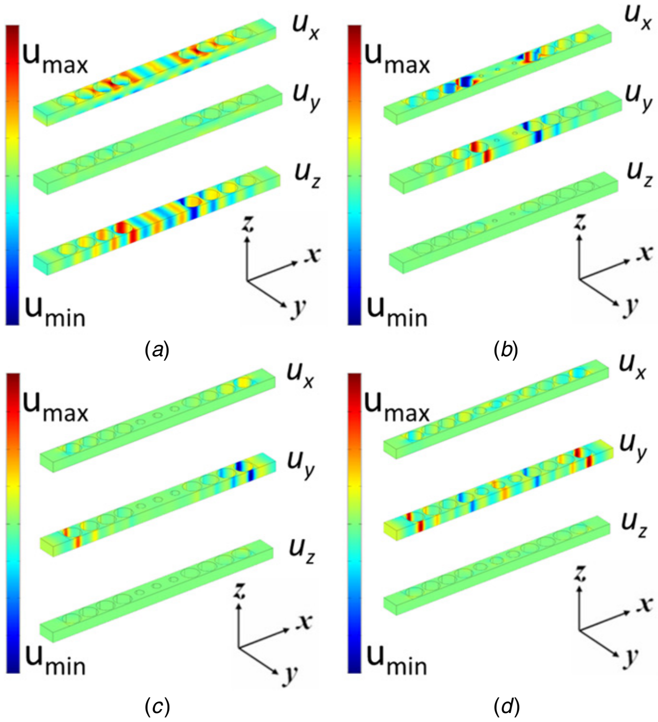

Figure 13. Simulated steady-state displacement profiles of (*a*) the Fabry-Perot PnC resonator, (*b*) the PnC resonator with reduced central-hole radii of $r' = 2\ \mu$m, (*c*) the PnC resonator with reduced central-hole radii of $r' = 4\ \mu$m, (*d*) the PnC resonator with reduced central-hole radii of $r' = 6\ \mu$m. The u_x, u_y and u_z represent the displacement vector components in the *x*, *y*, and *z* directions, respectively. The colour bar indicates the amplitude of displacements in an arbitrary unit, with extreme red representing the maximum displacement (maximum displacement amplitude in the positive direction) and extreme blue representing the minimum displacement (maximum displacement amplitude in the negative direction).

and $r' = 6\ \mu$m, respectively. The bands of interest which are selected are the bands which correspond to the resonant frequencies shown in figure 11 when $k_y = 0$. In other words, the frequency of the bands of interest when $k_y = 0$ should be the same as the simulated resonant frequencies in figure 11 for all four PnC resonators. As such, the selected bands of interest which correspond to the resonant peaks shown in figure 11 are labelled using blue arrows in all the sub-figures of figure 12. From the slopes of the bands, we can see that the selected bands in the calculated band structures agree quite with the experimental results. For example, the PnC resonator with $r' = 2\ \mu$m has the highest quality factor among all the cases, as shown in figure 10(*b*). Correspondingly, the case of $r' = 2\ \mu$m also has the flattest band when $k_y = 0$ among the four cases. Since it has the flattest band, the group velocity of the elastic waves along the *y* direction is slowest due to the slow sound effect. As a result, the amount of energy loss is smallest and thus the highest quality factor achieved. On the contrary, for the case of the Fabry–Perot resonator, it has the steepest band among the four cases as shown in figure 12(*a*), thus the quality factor for this case is also the lowest since the amount of energy loss is largest, as shown in figure 10(*a*). For the PnC resonators with $r' = 4\ \mu$m and $r' = 6\ \mu$m, the slope of the selected bands which correspond to the simulated resonant frequencies also agree well with the experimental results.

With the supercells which were built for the analysis of resonant frequencies, the steady-state displacement profiles of the structures at their respective resonant frequencies in the *x*, *y* and *z* directions of all designed PnC resonators are analysed by the FEM method. Again, periodic boundary conditions are applied along the *y* direction. As elastic waves in the silicon plate propagate by the interactions among the silicon atoms when they are displaced from their equilibrium positions, the energy stored in any solid structure is then associated with the displacements of the silicon atoms within the silicon plate. Thus, information about the energy distribution along the structure can be obtained by analysing the steady-state displacement profiles of the structures at their respective resonant frequencies.

The simulated steady-state displacement profiles for the case of the Fabry-Perot resonator is shown in figure 13(*a*), while figures 13(*b*)–(*d*) show the simulated steady-state displacement profiles for the PnC resonators with reduced central-hole radii of $r' = 2\ \mu$m, $r' = 4\ \mu$m, and $r' = 6\ \mu$m, respectively, under their respective resonant frequencies. The u_x, u_y and u_z represent the displacement vector components in the *x*, *y*, and *z* directions, respectively. The colour bar indicates the amplitude of displacements in an arbitrary unit, where extreme red represents the maximum displacement (maximum displacement amplitude in the positive direction) and extreme blue represents the minimum displacement (maximum displacement amplitude in the negative direction). One point to note here is the displacement which the colour bar represents is in an arbitrary unit, which means the u_{max} and u_{min} for the four cases are different. Therefore, from the steady-state displacement profiles we can only get information about the energy distribution along the single structure.

From the steady-state displacement profiles shown in figure 13, it can be easily seen that the steady-state displacement profile for the Fabry-Perot PnC resonator (figure 13(*a*)) is completely different from the PnC resonators with reduced central-hole radii (figures 13(*b*)–(*d*)). For the case of the Fabry–Perot resonator (figure 13(*a*)), the displacement profiles are concentrated in the x and z directions and almost no displacements can be observed along the y direction. This is actually the displacement profiles of a typical Fabry–Perot resonant mode. However, for the cases of PnC resonators with reduced central-hole radii (figures 13(*b*)–(*d*)), the Fabry-Perot resonant mode is destroyed and the displacement profiles are concentrated along the y direction and the displacement along the x and z directions is minimum.

For the case whereby the displacement vector components along the y direction are mainly distributed at the central defected region (e.g., figure 13(*b*)), the energy of the structures are concentrated at the central defect region. As such, the energy is better confined in the central defect region and little amount of energy is lost, leading to the high quality factor obtained. On the other hand, a lower quality factor is expected for the case whereby the displacement vector components along the y direction are not concentrated in the central defected region (e.g., figure 13(*c*)). For these cases, the energy is confined poorly in the central defect region and a large amount of energy is lost, resulting in a lower quality factor expected.

As compared to the cavity-mode Fabry–Perot resonators and Bloch-mode resonators, the defects are introduced by partially modifying the perfect PnC structures instead of completely removing several rows of air holes, the quality factor can be improved as a result of the significantly reduced scattering loss. The measured quality factors agree excellently with the calculated defected band structure and the phenomenon can be explained very well using the slow sound effect along the lateral direction, as indicated by the flat bands in the calculated defected band structure.

5. Conclusion

In this paper, micromechanical PnC resonators with various reduced central-hole radii have been explored and characterized. Experimental data for three designs of PnC resonators with central-hole radii of $r' = 2\ \mu$m, $r' = 4\ \mu$m, and $r' = 6\ \mu$m are reported. These designed PnC resonators are made from a 2D PnC slab of square lattice, which is fabricated from a free-standing silicon plate of 10 μm thickness using a CMOS-compatible process. The microfabricated PnC resonators with reduced central-hole radii are characterized in terms of the resonant frequency, quality factor, as well as insertion loss and the experimental results are discussed by analysing the simulated transmission spectra, the defected band structures, and the steady-state displacement profiles of the structures at their respective resonant frequencies. Good agreement was found between the simulation results and experimental data. The designed PnC resonators with reduced central-hole radii have higher resonant frequencies and higher quality factors as compared to their normal Fabry-Perot counterpart, with the (*f*-*Q*) product of as high as 2.96×10^{11} achieved which is among the highest for silicon resonators operating in air.

Acknowledgments

This work was partially supported by the Science and Engineering Research Council of A*STAR (Agency for Science, Technology and Research), Singapore, under grant number: SERC 1220103064 and SERC 1021010022 and the NRF-CRP001-057 Program—'Self-powered body sensor network for disease management and prevention oriented healthcare' under R-263-000-A27-281 from National Research Foundation (NRF), Singapore; and National Science Council NSC 101-2221-E-018-013, Taiwan.

References

[1] Sigalas M and Economou E N 1993 Band-structure of elastic-waves in 2-dimensional systems *Solid State Commun.* **86** 141–3

[2] Kushwaha M S, Halevi P, Dobrzynski L and Djafarirouhani B 1993 Acoustic band structure of periodic elastic composites *Phys. Rev. Lett.* **71** 2022–5

[3] Kushwaha M S, Halevi P, Martinez G, Dobrzynski L and Djafarirouhani B 1994 Theory of acoustic band structure of periodic elastic composites *Phys. Rev.* B **49** 2313–22

[4] Benchabane S, Khelif A, Rauch J Y, Robert L and Laude V 2006 Evidence for complete surface wave band gap in a piezoelectric phononic crystal *Phys. Rev. E* **73** 065601

[5] El-Kady I, Olsson R H and Fleming J G 2008 Phononic band-gap crystals for radio frequency communications *Appl. Phys. Lett.* **92** 233504

[6] Khelif A, Hsiao F L, Choujaa A, Benchabane S and Laude V 2010 Octave omnidirectional band gap in a three-dimensional phononic crystal *IEEE Trans. Ultrason. Ferroelectr. Freq. Control* **57** 1621–5

[7] Mohammadi S, Eftekhar A A, Khelif A, Hunt W D and Adibi A 2008 Evidence of large high frequency complete phononic band gaps in silicon phononic crystal plates *Appl. Phys. Lett.* **92** 1905

[8] Mohammadi S, Eftekhar A A, Khelif A, Moubchir H, Westafer R, Hunt W D and Adibi A 2007 Complete phononic bandgaps and bandgap maps in two-dimensional silicon phononic crystal plates *Electron. Lett.* **43** 898–9

[9] Pennec Y, Djafari-Rouhani B, Larabi H, Vasseur J and Hladky-Hennion A C Phononic crystals and manipulation of sound *Phys. Status Solidi C* **6** 2080–5

Sheregii E M, Gebicki W and Azhniuk (ed) Y M 2009 (Weinheim: Wiley-VCH) pp 2080–5
[10] Vasseur J O, Deymier P A, Chenni B, Djafari-Rouhani B, Dobrzynski L and Prevost D 2001 Experimental and theoretical evidence for the existence of absolute acoustic band gaps in two-dimensional solid phononic crystals *Phys. Rev. Lett.* **86** 3012–5
[11] Wu T T, Wu L C and Huang Z G 2005 Frequency band-gap measurement of two-dimensional air/silicon phononic crystals using layered slanted finger interdigital transducers *J. Appl. Phys.* **97** 094916
[12] Olsson R H, El-Kady I F, Su M F, Tuck M R and Fleming J G 2008 Microfabricated VHF acoustic crystals and waveguides *Sensors Actuators* A **145** 87—93
[13] Gorishnyy T, Ullal C K, Maldovan M, Fytas G and Thomas E L 2005 Hypersonic phononic crystals *Phys. Rev. Lett.* **94** 115501
[14] Lai Y and Zhang Z Q 2003 Large band gaps in elastic phononic crystals with air inclusions *Appl. Phys. Lett.* **83** 3900–2
[15] Achaoui Y, Khelif A, Benchabane S, Robert L and Laude V 2011 Experimental observation of locally-resonant and bragg band gaps for surface guided waves in a phononic crystal of pillars *Phys. Rev.* B **83** 104201
[16] Khelif A, Achaoui Y, Benchabane S, Laude V and Aoubiza B 2010 Locally resonant surface acoustic wave band gaps in a two-dimensional phononic crystal of pillars on a surface *Phys. Rev.* B **81** 214303
[17] Wu T-T, Huang Z-G, Tsai T-C and Wu T-C 2008 Evidence of complete band gap and resonances in a plate with periodic stubbed surface *Appl. Phys. Lett.* **93** 111902
[18] Mohammadi S, Eftekhar A A, Hunt W D and Adibi A 2008 Demonstration of large complete phononic band gaps and waveguiding in high-frequency silicon phononic crystal slabs *IEEE Int. Symp. Frequency Control* pp 768–72
[19] Hou Z L and Assouar B M 2009 Numerical investigation of the propagation of elastic wave modes in a one-dimensional phononic crystal plate coated on a uniform substrate *J. Phys. D: Appl. Phys.* **42** 085103
[20] Gomopoulos N, Maschke D, Koh C Y, Thomas E L, Tremel W, Butt H J and Fytas G 2010 One-dimensional hypersonic phononic crystals *Nano Lett.* **10** 980–4
[21] Hladky-Hennion A-C, Granger C, Vasseur J and de Billy M 2010 Propagation of elastic waves in one-dimensional periodic stubbed waveguides *Phys. Rev.* B **82** 104307
[22] Hsiao F-L, Khelif A, Moubchir H, Choujaa A, Chen C-C and Laude V 2007 Waveguiding inside the complete band gap of a phononic crystal slab *Phys. Rev. E* **76** 056601
[23] Kuo N K, Zuo C J and Piazza G 2009 Microscale inverse acoustic band gap structure in aluminum nitride *Appl. Phys. Lett.* **95** 093501
[24] Khelif A, Deymier P A, Djafari-Rouhani B, Vasseur J O and Dobrzynski L 2003 Two-dimensional phononic crystal with tunable narrow pass band: application to a waveguide with selective frequency *J. Appl. Phys.* **94** 1308–11
[25] Khelif A, Choujaa A, Djafari-Rouhani B, Wilm M, Ballandras S and Laude V 2003 Trapping and guiding of acoustic waves by defect modes in a full-band-gap ultrasonic crystal *Phys. Rev.* B **68** 214301
[26] Khelif A, Mohammadi S, Eftekhar A A, Adibi A and Aoubiza B 2010 Acoustic confinement and waveguiding with a line-defect structure in phononic crystal slabs *J. Appl. Phys.* **108** 084515
[27] Oudich M, Assouar M B and Hou Z 2010 Propagation of acoustic waves and waveguiding in a two-dimensional locally resonant phononic crystal plate *Appl. Phys. Lett.* **97** 193503
[28] Gu Y W, Luo X D and Ma H R 2009 Low frequency elastic wave propagation in two dimensional locally resonant phononic crystal with asymmetric resonator *J. Appl. Phys.* **105** 044903
[29] Vasseur J O, Hladky-Hennion A C, Djafari-Rouhani B, Duval F, Dubus B, Pennec Y and Deymier P A 2007 Waveguiding in two-dimensional piezoelectric phononic crystal plates *J. Appl. Phys.* **101** 114904
[30] Benchabane S, Khelif A, Choujaa A, Djafari-Rouhani B and Laude V 2005 Interaction of waveguide and localized modes in a phononic crystal *Europhys. Lett.* **71** 570–5
[31] Wang N, Hsiao F-L, Palaniapan M and Lee C 2011 Silicon two-dimensional phononic crystal resonators using alternate defects *Appl. Phys. Lett.* **99** 234102
[32] Wang N, Hsiao F L, Tsai J M, Palaniapan M, Kwong D L and Lee C 2012 Investigation on the optimized design of alternate-hole-defect for 2D phononic crystal based silicon microresonators *J. Appl. Phys.* **112** 024910
[33] Wang N, Tsai J M L, Hsiao F L, Soon B W, Kwong D L, Palaniapan M and Lee C 2012 Micromechanical resonators based on silicon two-dimensional phononic crystals of square lattice *J. Microelectromech. Syst.* **21** 801–10
[34] Wang N, Tsai J M, Hsiao F L, Soon B W, Kwong D L, Palaniapan M and Lee C 2011 Experimental Investigation of a cavity-mode resonator using a micromachined two-dimensional silicon phononic crystal in a square lattice *IEEE Electron Device Lett.* **32** 821–3
[35] Nguyen C T C 2007 MEMS technology for timing and frequency control *IEEE Trans. Ultrason. Ferroelectr. Freq. Control* **54** 251–70
[36] Ryder S, Lee K B, Meng X F and Lin L W 2004 AFM characterization of out-of-plane high frequency microresonators *Sensors Actuators* A **114** 135–140
[37] Joachim D and Liwei L 2003 Characterization of selective polysilicon deposition for MEMS resonator tuning *J. Microelectromech. Syst.* **12** 193–200
[38] Khine L and Palaniapan M 2009 High-Q bulk-mode SOI square resonators with straight-beam anchors *J. Micromech. Microeng.* **19** 015017
[39] Wang K, Wong A C and Nguyen C T C 2000 VHF free-free beam high-Q micromechanical resonators *J. Microelectromech. Syst.* **9** 347–60
[40] Yu-Wei L, Sheng-Shian L, Yuan X, Zeying R and Nguyen C T C 2005 Vibrating micromechanical resonators with solid dielectric capacitive transducer gaps *IEEE Int. Symp. Frequency Control* pp 128–34
[41] Pourkamali S, Hashimura A, Abdolvand R, Ho G K, Erbil A and Ayazi F 2003 High-Q single crystal silicon HARPSS capacitive beam resonators with self-aligned sub-100-nm transduction gaps *J. Microelectromech. Syst.* **12** 487–96
[42] Ho G K, Abdolvand R, Sivapurapu A, Humad S and Ayazi F 2008 Piezoelectric-on-silicon lateral bulk acoustic wave micromechanical resonators *J. Microelectromech. Syst.* **17** 512–20
[43] Piazza G, Stephanou P J and Pisano A P 2006 Piezoelectric aluminum nitride vibrating contour-mode MEMS resonators *J. Microelectromech. Syst.* **15** 1406–18
[44] Piazza G, Stephanou P J and Pisano A P 2007 Single-chip multiple-frequency AlN MEMS filters based on contour-mode piezoelectric resonators *J. Microelectromech. Syst.* **16** 319–28
[45] Yablonovitch E 1987 Inhibited spontaneous emission in solid-state physics and electronics *Phys. Rev. Lett.* **58** 2059–62
[46] John S 1987 Strong localization of photons in certain disordered dielectric superlattices *Phys. Rev. Lett.* **58** 2486–9
[47] McCutcheon M W and Loncar M 2008 Design of a silicon nitride photonic crystal nanocavity with

a quality factor of one million for coupling to a diamond nanocrystal *Opt. Express* **16** 19136–45

[48] Lee C, Thillaigovindan J, Chen C C, Chen X T, Chao Y T, Tao S H, Xiang W F, Yu A B, Feng H H and Lo G Q 2008 Si nanophotonics based cantilever sensor *Appl. Phys. Lett.* **93** 113113

[49] Lalanne P and Hugonin J P 2003 Bloch-wave engineering for high-Q, small-V microcavities *IEEE J. Quantum Electron.* **39** 1430–8

[50] Hsiao F L, Khelif A, Moubchir H, Choujaa A, Chen C C and Laude V 2007 Complete band gaps and deaf bands of triangular and honeycomb water-steel phononic crystals *J. Appl. Phys.* **101** 044903